Research Square

Preprints are preliminary reports that have not undergone peer review.
They should not be considered conclusive, used to inform clinical practice,
or referenced by the media as validated information.

Transient metabolon dynamics tune enzyme specificity

Toru Nakayama

toru.nakayama.e5@tohoku.ac.jp

Tohoku University https://orcid.org/0000-0002-5275-4731

Riki Imaizumi

Tohoku University

Toshiyuki Waki

Tohoku University

Yoshikazu Hattori

Tokushima University https://orcid.org/0000-0002-0013-5584

Kohei Takeshita

RIKEN SPring-8 Center

Miru Sumita

Kanazawa University

Kazutomo Kawaguchi

Kanazawa University

Hiroyuki Kumeta

Hokkaido University

Kenichi Umeda

Kanazawa University

Kyohei Sato

Tohoku University

Taro Yanai

Kanazawa University

Hiroaki Matsuura

University of Hyogo

Takeshi Yokoyama

Tohoku University

Risa Omura

Kanazawa University

Kayo Nakatani

Kanazawa University

Naoki Sakai

Japan Synchrotron Radiation Research Institute
Yukimura Kawagiwa
Tohoku University
Yamato Doi
Tohoku University
Aoi Yasuda
Kanazawa University
Takuya Nakano
Tohoku University
Kaichi Uno
Tohoku University
Kunihiro Yoshida
Kanazawa University
Misato Tsunashima
Tohoku University
Tomohide Saio
Tokushima University
Yoshikazu Tanaka
Tohoku University
Seiji Takahashi
Tohoku University
Noriyuki Kodera
Kanazawa University https://orcid.org/0000-0003-4880-8423
Kunishige Kataoka
Kanazawa University https://orcid.org/0000-0001-7096-7565
Masaki Yamamoto
RIKEN SPring-8 Center
Satoshi Yamashita
Kanazawa University

Article

Keywords:

Posted Date: September 23rd, 2025

DOI: https://doi.org/10.21203/rs.3.rs-7450846/v1

License: This work is licensed under a Creative Commons Attribution 4.0 International License.
Read Full License

Additional Declarations: There is **NO** Competing Interest.

Version of Record: A version of this preprint was published at Nature Catalysis on June 15th, 2026. See the published version at https://doi.org/10.1038/s41929-026-01551-6.

Transient metabolon dynamics tune enzyme specificity

Authors: Riki Imaizumi[1,2,11], Toshiyuki Waki[2,11], Yoshikazu Hattori[3], Kohei Takeshita[4,5], Miru Sumita[1], Kazutomo Kawaguchi[6], Hiroyuki Kumeta[7], Kenichi Umeda[8], Kyohei Sato[9], Taro Yanai[1], Hiroaki Matsuura[5], Takeshi Yokoyama[9], Risa Omura[8], Kayo Nakatani[8], Naoki Sakai[10], Yukimura Kawagiwa[2], Yamato Doi[2], Aoi Yasuda[1], Takuya Nakano[2], Kaichi Uno[2], Kunihiro Yoshida[1], Misato Tsunashima[2], Tomohide Saio[3], Yoshikazu Tanaka[9], Seiji Takahashi[2], Noriyuki Kodera[8], Kunishige Kataoka[1], Masaki Yamamoto[4], Satoshi Yamashita[1]*, Toru Nakayama[2]*

Affiliations:

[1] Graduate School of Natural Science and Technology, Kakuma, Kanazawa University; Kanazawa, Ishikawa 920-1192, Japan.

[2] Graduate School of Engineering, Tohoku University; Sendai, Miyagi 980-8579, Japan.

[3] Institute of Advanced Medical Sciences, Tokushima University; Tokushima 770-8503, Japan.

[4] RIKEN SPring-8 Center; Sayo-cho, Sayo-gun, Hyogo 679-5148, Japan.

[5] Graduate School of Life Science, University of Hyogo; Ako-gun, Hyogo 678-1205, Japan.

[6] Institute of Science and Engineering, Kanazawa University; Kanazawa, Ishikawa 920-1192, Japan.

[7] Faculty of Advanced Life Science, Hokkaido University; Sapporo, Hokkaido 060-0810, Japan.

[8] Nano Life Science Institute, Kanazawa University; Kakuma, Kanazawa, Ishikawa 920-1192, Japan.

[9] Graduate School of Life Sciences, Tohoku University; Sendai, Miyagi 980-8577, Japan.

[10] Japan Synchrotron Radiation Research Institute (JASRI); Sayo-cho, Sayo-gun, Hyogo 679-5146, Japan.

[11] These authors contributed equally to this work

*e-mail: yamashita@se.kanazawa-u.ac.jp, toru.nakayama.e5@tohoku.ac.jp

Abstract: Cells achieve metabolic precision by assembling enzymes into dynamic complexes, but the regulatory mechanism of these metabolons is unclear. Here, we characterize the chalcone synthase (CHS)–chalcone isomerase-like protein (CHIL) complex, a key component of flavonoid metabolons. Whereas crystallography provides a static view, our analyses reveal that CHS undergoes rapid, reversible binding cycles with CHIL that regulate catalysis in real time. CHIL removes coenzyme A, an inhibitor of Claisen cyclization, transiently reshapes the CHS active site, and guides the tetraketide intermediate toward productive cyclization, thereby suppressing derailment byproducts. These findings demonstrate a previously unproven and generalizable regulatory effect in metabolons: guided active-site tuning via transient enzyme association. This concept enhances our understanding of metabolon function and opens new avenues for synthetic biology and metabolic engineering.

(Introduction)

Metabolons are transient and dynamic supramolecular complexes consisting of enzymes that mediate sequential reactions and related proteins in a metabolic pathway[1,2]. Metabolons were first identified in primary metabolism-related pathways in animals[3] and have since been detected in connection with various metabolic processes in microorganisms, plants, and animals[4-7]. Metabolons offer several advantages in metabolism, including higher local concentrations of enzymes and their substrates[8], metabolite channeling[9,10], and greater enzyme specificity through protein–protein interactions[11,12]. However, because of the dynamic and transient nature of metabolons, it is difficult to elucidate how their enzymes and proteins assemble at the atomic level to confer these advantages[2,13].

The formation of metabolons is well exemplified by the flavonoid biosynthetic pathway in land plants. Flavonoids are a class of plant metabolites characterized by a

general C_6–C_3–C_6 structure with extensive structural diversity[14,15] and play crucial roles in plant survival and reproduction[14,15], while also providing various health benefits to humans (**Supplementary Fig. 1**)[16]. Flavonoid biosynthesis is initiated by chalcone synthase (CHS), a plant-specific type III polyketide synthase[17,18]. CHS catalyzes the formation of 2′,4,4′,6′-tetrahydroxychalcone (THC; **Fig. 1A**, compound **3**) from *p*-coumaroyl-CoA **1** and three molecules of malonyl-CoA **2** (**Scheme 1**) *via* three consecutive intermolecular Claisen condensations (**Fig. 1A**, red arrows i–iii) followed by intramolecular Claisen cyclization (red arrow iv) of the tetraketide intermediate (T-i, **6**):

p-coumaroyl-CoA + 3 malonyl-CoA → THC + 4 CoA + 3 CO_2 (**Scheme 1**).

THC is a crucial precursor for flavonoid biosynthesis and is subsequently converted to (2*S*)-naringenin **8** by chalcone isomerase (CHI), leading to the production of various flavonoid classes in a lineage-specific manner (**Fig. 1A**). THC and (2*S*)-naringenin are structural isomers and are collectively referred to as chalconoids (CLC). CHS, CHI, and other downstream flavonoid-related enzymes form a flavonoid metabolon (**Supplementary Fig. 2**)[19-21], which provides an ideal system to investigate metabolon function.

The refinement of enzyme specificity through protein–protein interactions is one of the most significant aspects of metabolon formation in plant metabolism. Enzymes in specialized metabolic pathways in plants, including those in the flavonoid pathway, often exhibit "catalytic promiscuity," resulting in the catalysis of reactions without known biological or physiological relevance[12,22,23]. This promiscuity is believed to serve as a foundation for the evolution of new enzyme functions and metabolic pathways[22,23]. However, if left uncorrected, it can reduce the metabolic efficiency of plants. CHS exemplifies this catalytic promiscuity, producing byproducts such as *p*-coumaroyltriacetic acid lactone (CTAL, **9**), which can constitute 50%–90% of the products of CHS-catalyzed reactions *in vitro* (**Fig. 1B**; see also **Fig. 1A**, blue arrow v)[11,12]. CTAL formation is enhanced by coenzyme A (CoA), a reaction product, with the THC:CTAL ratio decreasing from 80:20 to 0:100 (mol%) as the CoA concentration increases[24]. Because CTAL is inert

as a flavonoid precursor, this intrinsic promiscuity of CHS may reduce the efficiency of flavonoid biosynthesis and compromise flavonoid-mediated responses in land plants if not rectified.

The CHI-like protein (CHIL, a type IV member of the chalcone isomerase family), which shows structural similarity to CHI but lacks CHI enzyme activity[25], is a component of flavonoid metabolons **Supplementary Fig. 2**)[11]. In flavonoid metabolons, CHIL binds to CHS, thereby enhancing THC production and restricting CTAL formation, which mitigates the promiscuous activity of CHS (**Fig. 1AB**). CHIL-encoding genes are ubiquitous in land plant genomes, indicating that this role of CHIL in flavonoid metabolons is highly conserved and that the optimization of the influx of substrates from the general phenylpropanoid pathway into the flavonoid pathway is critical (**Fig. 1A**)[11]. However, because of the fragile nature of protein complexes in metabolons, it is unclear how CHIL interacts with CHS to fulfill this important function.

Here, we present the structural and dynamic basis for how the CHS–CHIL complex achieves metabolic precision. We demonstrate that transient, rapid protein-protein interactions mediate a previously unproven regulatory effect—Guided Active-site Tuning *via* Transient Enzyme Association (GATE)—a fundamental concept that advances our understanding of metabolon function and offers new avenues for metabolic engineering.

Results

Structure of the CHS–CHIL complex

We aimed to isolate CHS–CHIL complexes from three plant species: *Physcomitrella patens*, *Arabidopsis thaliana*, and soybean (*Glycine max*). CHS and CHIL from *P. patens* (designated PpCHS and PpCHIL; Phytozome v12.1 loci Pp3c24_13120 and Pp3c426_4040, respectively)[11,26,27] were expressed in *Escherichia coli* and purified to homogeneity. When an equimolar mixture (120 μM for each monomer) of PpCHS (a homodimer of a 45-kDa subunit) and PpCHIL (25 kDa) was subjected to size-exclusion chromatography (SEC) in the absence of NaCl, a prominent shoulder peak corresponding to a complex of approximately 230 kDa was observed, consistent with the formation of a

PpCHS–PpCHIL complex (**Supplementary Fig. 3A**). Under the same conditions, CHS and CHIL from *A. thaliana* formed a comparable amount of complex, whereas only a negligible amount was formed in the soybean-derived mixture (**Supplementary Fig. 3BC**), demonstrating interspecies variability in CHS–CHIL complex stability. However, in the presence of 0.2 M NaCl, complex formation was minimal for all three species (**Supplementary Fig. 3CD**), indicating the salt-sensitive nature of the interaction.

The PpCHS–PpCHIL complex purified under low-salt conditions was subjected to structural analysis. Crystals of the complex were obtained, and its structure was determined at 1.9 Å resolution *via* molecular replacement (PDB:9KAH) (**Supplementary Table 1**). We also resolved the structures of PpCHIL alone (PDB:9KAI) and CoA-bound PpCHS (PpCHS–CoA; PDB:9KAJ) (**Supplementary Table 1**). The PpCHS–PpCHIL complex consisted of two identical PpCHS subunits (designated mol_A and mol_B, each with 397 residues) and two PpCHIL monomers (212 residues each), forming a 2:2 heterotetramer (**Fig. 2A**). Each PpCHIL monomer interacted with both subunits of the PpCHS dimer (**Fig. 2A**).

A key feature of the interaction between two proteins was found to be the insertion of the β-hairpin (βHP) of PpCHIL (Thr34^{PpCHIL}–Phe45^{PpCHIL}) into the CoA-binding tunnel of PpCHS (**Fig. 2B**), suggesting competitive binding between CHIL and CoA (a reaction product; see **Fig. 1A**). This interaction was stabilized primarily by hydrophobic contacts (**Supplementary Fig. 4A**). Additionally, electrostatic complementarity contributed to the interaction: a lysine triad on the PpCHIL surface (Lys97^{PpCHIL}, Lys100^{PpCHIL}, and Lys144^{PpCHIL}) faced a negatively charged patch on PpCHS (**Supplementary Fig. 4B**). Specifically, Lys97^{PpCHIL} interacted with Asp213^{PpCHS_A} and His272^{PpCHS_A}; Lys100^{PpCHIL} with Asp102^{PpCHS_B}; and Lys144^{PpCHIL} with Asn210^{PpCHS_A} (superscripts ^{PpCHS_A} and ^{PpCHS_B} denote mol_A and mol_B of dimeric PpCHS, respectively) (**Fig. 2C**). Notably, Asp213^{PpCHS} was located on a mobile α-helix (H9; see **Supplementary Fig. 5** for the secondary structures of CHS), as previously described for soybean CHS (GmCHS1)[24], and this interaction likely stabilizes that helix in PpCHS. Furthermore, α-helices H4 and H5 of PpCHIL contributed to the interface with mol_B of PpCHS (**Fig. 2C**) (see **Supplementary**

Fig. 6 for the secondary structures of CHIL). PpCHIL binding also induced the formation of an inter-subunit salt bridge between Asp257^{PpCHS_A} and Lys152^{PpCHS_B} (**Supplementary Fig. 7**), which may further stabilize the PpCHS dimer.

Interactions between PpCHIL and PpCHS induced significant conformational changes in both proteins. In PpCHIL, the β-HP underwent substantial rearrangement (**Fig. 3A**). For PpCHS, the backbone conformations of residues forming the active-site cavity (**Fig. 3B**) varied according to the ligand bound (PpCHIL *versus* CoA). This active-site cavity included the CoA-binding tunnel, the CLC-binding pocket, which accommodated the final product, THC, and a tunnel-like space[18,24] (see **Fig. 3B**). This tunnel-like space is a recurring feature, also identified in the structures of CHSs from other plants such as soybean[18]. A comparison of the structures of PpCHS–PpCHIL and PpCHS–CoA revealed significant differences in the dihedral angles (ϕ and ψ) of the amino acids within the active-site cavity (**Supplementary Fig. 8**). Notably, the PpCHS–CoA active-site cavity featured an expanded tunnel-like space near the CLC-binding pocket that showed no significant expansion in either PpCHS–PpCHIL or apo PpCHS (PpCHS without a ligand; PDB ID:6DX7)[28] (**Fig. 3B**). Additionally, within the active-site cavity, certain residues comprised the K-loop (Leu273^{PpCHS}–Asp276^{PpCHS}). This flexible segment has been hypothesized to alternate between open and closed conformations during catalysis[24] (**Supplementary Fig. 9**), and its conformation was affected by both CHIL and CoA binding (**Supplementary Fig. 9**). In the PpCHS–PpCHIL complex, the K-loop adopted an open conformation, with the side chain of Lys275^{PpCHS} pointing away from the CoA-binding tunnel (**Fig. 2B**). In contrast, in the PpCHS–CoA structure, the K-loop had a closed conformation, and Lys275^{PpCHS} directly interacted with the bound CoA (**Fig. 2B**; **Supplementary Fig. 9**).

These structural observations imply that PpCHIL modulates the conformational dynamics of the PpCHS active-site cavity. Consistent with this, normalized B-factor (B′-factor) analysis[29] of the PpCHS–CoA structure showed a high level of mobility of both the K-loop and the active-site cavity. In contrast, these regions exhibited no such flexibility in the PpCHS–PpCHIL complex (**Supplementary Fig. 10AB**). Whereas the apo PpCHS also

showed moderately elevated B′-factor values in these regions, there were substantially lower than in the PpCHS–CoA structure (**Supplementary Fig. 10B**). These data suggest that the CHS active-site cavity alternates between a flexible (F) state and a more stable (S) state during the CHS catalytic cycle, with apo CHS existing in an intermediate, unliganded (U) state. CoA binding promotes the formation of the F state, whereas CHIL binding induces the S state. These conformational states likely influence the conformation of T-i (**Fig. 1A**, **6**) that is formed during catalysis, which affects the product specificity of CHS. This is corroborated by the results of the computational studies described below.

Structural conservation of CHS–CHIL and its dynamics in solution

The conservation of the mode of CHS-CHIL complex formation across land plants was next evaluated by sequence comparison, computational structure prediction, and mutation studies. Sequence comparison revealed that Lys97^{PpCHIL} and Lys100^{PpCHIL} of PpCHIL and Asp213^{PpCHS}, His272^{PpCHS}, and Asp102^{PpCHS} of PpCHS were highly conserved among plant species, whereas Lys144^{PpCHIL} and Asn210^{PpCHS} were less conserved (**Supplementary Fig. 5** and **Supplementary Fig. 6**). Additionally, the amino acid sequences of the βHPs of CHILs were not necessarily conserved (**Supplementary Fig. 6**). The structural conservation of the CHS-CHIL complexes in land plants was confirmed by predicting the CHS–CHIL complex structures of other land plants using AlphaFold2 (**Supplementary Fig. 11**). The functional importance of the two conserved lysine residues (Lys97^{PpCHIL} and Lys100^{PpCHIL}) and the amino acid residues within βHP (Thr34^{PpCHIL}, Glu37^{PpCHIL}, Ile38^{PpCHIL}, Glu39^{PpCHIL}, and Phe45^{PpCHIL}) for the binding of CHIL to CHS was confirmed using yeast two-hybrid assays[30-33] of the *P. patens*, *G. max*, and *A. thaliana* CHS–CHIL systems (**Supplementary Fig. 12**). We concluded that the following two primary interactions are involved in the CHS-CHIL complex formation, irrespective of plant origin: (1) polar interactions mediated by two highly conserved lysine residues in CHIL and (2) hydrophobic interactions between amino acid residues in the βHP domain of CHIL and residues located near the CoA-binding tunnel of CHS. The strength of the interaction between CHS and CHIL was influenced by the βHP domain amino acid sequence of CHIL

(**Supplementary Fig. 12**), at least in part explaining why CHS–CHIL complexes from different plants differ in their stability (see above). Moreover, the fact that only negligible amounts of CHS-CHIL complex were obtained during SEC in the presence of 0.2 M NaCl (see above, **Supplementary Fig. 3CD**) suggests that the CHS–CHIL complexes are formed mainly *via* electrostatic interactions. Considering the intracellular conditions of plant cells[34], in which electrolyte concentrations are typically 100–200 mM K^+ and 1–10 mM Na^+, it is highly likely that the CHS-CHIL complex is unstable *in vivo*, as for other metabolons. Thus, the X-ray crystal structure likely represents a transient "snapshot" of the bound state, capturing a moment within the dynamic association–dissociation process of these two proteins. The dissociation constant (K_d) of PpCHS–PpCHIL was determined to be 31.8 ± 1.5 μM in 20 mM HEPES–NaOH (pH 7.0) containing 150 mM NaCl and 0.1% Tween 20 (**Supplementary Table 2**; see also **Supplementary Fig. 13**) using microscale thermophoresis (MST) analysis[35,36]. In 200 mM HEPES–KOH (pH 7.5) containing 0.1% bovine serum albumin, biolayer interferometry (BLI) analysis[37] yielded a K_d value of 12.8 ± 0.7 μM (**Supplementary Table 2**; see also **Supplementary Fig. 14**) with association (k_{on}) and dissociation (k_{off}) constants of 1.68×10^5 $s^{-1}M^{-1}$ and 2.16 s^{-1}, respectively (**Supplementary Note 1**; see also **Supplementary Fig. 14**).

To gain deeper insight into the dynamic interaction between CHS and CHIL in solution, we performed nuclear magnetic resonance (NMR) analysis. We prepared ^{13}C- and ^{15}N-labeled PpCHIL and conducted a series of triple resonance experiments to determine the backbone amide resonances of 200 of the 212 amino acid residues of PpCHIL (**Supplementary Fig. 15A**). Subsequently, the interaction between PpCHS and PpCHIL was monitored by NMR in the absence or presence of 50 mM NaCl. In the absence of NaCl, most of the ^{15}N-PpCHIL resonances exhibited significant broadening upon the addition of 0.5 equivalents of PpCHS, with some nearly disappearing (**Supplementary Fig. 15B**). This suggests that the tight binding between PpCHIL and PpCHS results in the formation of a relatively large, slowly tumbling complex, and is consistent with the SEC data and crystal structure. However, in the presence of 50 mM NaCl, only a few PpCHIL resonances—specifically those corresponding to amino acid residues within βHP and

adjacent to the conserved Lys97^{PpCHIL} that interacts with PpCHS (*e.g.*, Thr40^{PpCHIL} and Ile96^{PpCHIL}, respectively)—exhibited chemical shift changes and line broadening upon the addition of 0.5 equivalents of PpCHS (**Fig. 3CD**; **Supplementary Fig. 15CD**). Notably, Thr40^{PpCHIL} and Ile96^{PpCHIL} are located at the interface with PpCHS in the X-ray crystal structure of the complex (**Fig. 3C**). These results confirm that the CHS-CHIL interaction interfaces identified *via* X-ray crystallography are also relevant in solution, as demonstrated using NMR analysis. The observed line broadening and chemical shift changes of these residues likely reflect exchange broadening, which can be attributed to the association–dissociation dynamics of the complex, highlighting the dynamic nature of the interaction between CHS and CHIL.

Guided active-site tuning *via* a transient enzyme association (GATE), revealed by computational studies

To determine how CHIL binding affects CHS catalysis, we performed computational simulations using AutoDock-GPU[38]. We docked a covalently bound T-i to Cys170 of PpCHS within the active-site cavity. We analyzed three distinct PpCHS structural states: the S state (PpCHS–PpCHIL), the F state (PpCHS–CoA), and the U state (apo PpCHS, without ligand) (see above).

These covalent docking simulations revealed a marked difference in the T-i conformation of the PpCHS–PpCHIL and PpCHS–CoA complexes (**Fig. 4AB**). In the PpCHS–PpCHIL complex, T-i adopted a compact conformation within the CLC-binding pocket, with C6–C1 and C5–C1 distances of 4.1 Å and 4.3 Å, respectively (**Fig. 4A**). Conversely, in the PpCHS–CoA complex, T-i was located in the tunnel-like space near the CLC-binding pocket and had an elongated conformation, with C6–C1 and O5–C1 distances of 5.0 Å and 4.5 Å, respectively (**Fig. 4B**). The docking energy distribution for T-i in the PpCHS–PpCHIL complex was closely centered around −10 kcal/mol (**Fig. 4A**), indicating strong and consistent stabilization, consistent with the S state of the surrounding environment. In contrast, the energy distribution for T-i in PpCHS–CoA was broader and included higher values (> −1.0 kcal/mol) (**Fig. 4B**), suggestive of less stable conformations.

This instability was attributed to T-i occupying the expanded tunnel-like space in the active-site cavity, which was in the F state. Importantly, the presence of bound CoA appeared to inhibit the accommodation of T-i in PpCHS–CoA; steric hindrance from the CoA molecule's thiol moiety limited the conformational change in T-i that is required for its entry to the CLC-binding pocket. The predicted T-i conformation and energy levels of apo PpCHS resembled those of the PpCHS–PpCHIL complex, although with a less sharply defined energy distribution (**Supplementary Fig. 16A**). These findings suggest that CHIL binding guides the conformation of the active-site cavity of CHS, orienting T-i for productive Claisen cyclization.

To further investigate, we performed 1,000-ps molecular dynamics (MD) simulations of T-i bound to PpCHS structures using GROMACS[39]. In the PpCHS–PpCHIL simulation, T-i consistently remained in the CLC-binding pocket (**Supplementary Fig. 16B**). Moreover, the distance between C6 and C1 of T-i remained significantly shorter than the O5–C1 distance throughout the simulation (**Fig. 4C**), supporting a stabilized Claisen cyclization geometry. Analysis of the dihedral angles of the T-i carbon atoms showed that C6–C1 Claisen cyclization was most favorable in the CHS–CHIL simulation (**Fig. 4D, Supplementary Fig. 16C**). Conversely, in the PpCHS–CoA simulation, T-i moved outside the CLC-binding pocket, maintaining an elongated conformation throughout in the tunnel-like space (**Supplementary Fig. 16B**). In this, the O5–C1 distance of T-i remained significantly shorter than the C6–C1 distance (**Fig. 4C**), suggesting a preference for lactonization over Claisen cyclization. Interestingly, in the apo PpCHS simulation, although T-i was located in the CLC-binding pocket and had a compact conformation (**Supplementary Fig. 16B**), its distance profiles resembled those for PpCHS–CoA (**Supplementary Fig. 16D**, see also **Supplementary Fig. 16E** for the results of the dihedral angle analysis of the T-i carbon atoms). Taken together, these findings strongly suggest that the conformation of T-i in the CHS–CHIL complex is stable and oriented favorably for C6–C1 Claisen cyclization (**Fig. 1A**, red arrow iv). In contrast, in the CHS–CoA complex, the T-i conformation appears unstable, owing to the presence of CoA, rendering it more liable to O5–C1 lactonization (blue arrow v).

Thus, both covalent docking and MD simulations indicated that CHIL binding modulates the T-i conformation to promote productive Claisen cyclization. Specifically, CHIL binding reshapes and stabilizes the CHS active-site cavity, guiding the intermediate along a favorable reaction pathway (**Fig. 5**). This process, which is mediated by transient protein–protein interactions within metabolons, exemplifies a regulatory effect that have never been proven so far in metabolons: Guided Active-site Tuning *via* Transient Enzyme association (GATE).

A kinetic gate: a rapid CHIL–CHS interaction regulates catalytic specificity

In metabolons, direct protein–protein interactions near the active sites of enzymes are crucial for processes such as substrate channeling[40], but they can also have inhibitory effects by physically obstructing the active site. To avoid this, metabolons are thought to rely on transient and weak interactions, but this has yet to be experimentally confirmed. However, the kinetic and thermodynamic data for the CHS-CHIL interaction and CHS catalysis presented below provide strong evidence for this model.

During CHS-catalyzed THC biosynthesis, four sequential Claisen condensations occur, with a molecule of CoA being released during each step (**Fig. 1A**, red arrows i–iv). These CoA molecules must be rapidly displaced from the CoA-binding tunnel to prevent them from acting as inhibitors and promoting the formation of unwanted byproducts [24]. Structural data have shown that when CoA is bound, the enzyme's active-site cavity favors the F state, which leads to the production of undesirable byproducts through O5–C1 lactonization of T-i. In contrast, CHIL binding induces the S state, which stabilizes a T-i conformation that is optimal for THC production. Therefore, efficient catalysis requires the active removal of CoA. The crystal structure of the PpCHS–PpCHIL complex revealed that the βHP region of CHIL occupies the CoA-binding tunnel (**Fig. 2B**), strongly suggesting that CHIL displaces the bound CoA during catalysis (**Supplementary Note 2**). However, this also means that CHIL competes with the CoA-ester substrates *p*-coumaroyl-CoA and malonyl-CoA for the CHS active site. This is why the weak binding between CHIL and CHS is critical to the regulatory role of CHIL; if the interaction were stronger, CHIL would

act as an inhibitor rather than a modulator. A critical aspect of CHIL function is that it must associate with and dissociate from CHS much more rapidly than the enzyme completes a catalytic cycle. To verify this, we performed kinetic analyses of PpCHS-catalyzed THC production both with and without PpCHIL (**Supplementary Table 3**), and found that the K_d for PpCHIL binding to PpCHS (32 μM *via* MST; 13 μM *via* BLI) were significantly higher than the Michaelis constants (K_m) of PpCHS for its CoA-ester substrates *p*-coumaroyl-CoA (3.8 μM) and malonyl-CoA (1.46 μM). Furthermore, the dissociation rate constant for the PpCHS–PpCHIL interaction (k_{off} = 2.16 s^{-1}, **Supplementary Table S2**) was two-to-three orders of magnitude higher than the enzyme's turnover rate (k_{cat}). Specifically, for *p*-coumaroyl-CoA, $k_{cat} = 2.63\times10^{-2}$ s^{-1}, and for malonyl-CoA, $k_{cat} = 3.45\times10^{-3}$ s^{-1} (**Supplementary Table 3**). These findings were consistent with the results of NMR analysis (see above) and confirm that CHIL binds to and dissociates from CHS far more frequently than CHS catalyzes a reaction. During these rapid binding and release events (**Fig. 5**), CHIL displaces CoA from the binding tunnel and reshapes the CHS active-site cavity. This action stabilizes the productive T-i conformation, thereby guiding the specificity of the less frequent catalytic events. As a result, CHIL increases the K_m values of CHS for its substrates while concurrently increasing its k_{cat} values, ultimately enhancing the overall catalytic efficiency (k_{cat}/K_m) for THC biosynthesis (**Supplementary Table 3**). This establishes CHIL as a dynamic gatekeeper of CHS specificity.

Conclusions

Our research provides the first structural evidence for how CHIL regulates CHS specificity, revealing a previously unproven, generalizable regulatory effect on enzyme catalysis within metabolons. We've named this effect the Guided Active-site Tuning via Transient Enzyme Association (GATE), and it is driven by the rapid, weak protein-protein interactions that are a hallmark of metabolon dynamics. Our findings suggest that these dynamic and transient enzyme-enzyme interactions—whether they occur near the active sites or in a more remote region—represent a fundamental mechanism for GATE. This work highlights how flexible enzymes can leverage dynamic metabolon formation to achieve precise regulatory control.

Ultimately, this concept advances our understanding of metabolic regulation and offers new avenues for engineering enzyme function, especially within modular biosynthetic systems such as polyketide synthases.

Materials and methods

Materials

The plasmid pColdI was obtained from Takara Bio (Otsu, Japan). *Escherichia coli* strains BL21 and BL21 (DE3) were obtained from Promega (Madison, WI, USA). THC was purchased from ChemFaces (Wuhan, China). Malonyl-CoA, CoA, *trans*-*p*-coumaric acid, imidazole, ATP, and isopropyl β-D-1-thiogalactopyranoside (IPTG) were purchased from Nacalai Tesque (Kyoto, Japan). High-performance liquid chromatography (HPLC)-grade acetonitrile and formic acid were obtained from Sigma-Aldrich Japan (Tokyo, Japan). Polyethylene glycols (PEG) 400, 3350, 6000, and 8000 were obtained from Hampton Research (Aliso Viejo, CA, USA). Recombinant AtCHS, AtCHIL, GmCHS1, and GmCHIL proteins were expressed in *E. coli* BL21 and purified as described previously[11,18]. *p*-Coumaroyl-CoA was synthesized from *trans*-*p*-coumaric acid, CoA, and ATP via a 4-coumaric acid:CoA ligase (4CL)-catalyzed reaction, as follows. The reaction mixture (final volume, 100 mL) consisted of 1 mM *trans*-*p*-coumaric acid, 1 mM CoA, 10 mM ATP, and 433 μg of recombinant 4CL from snapdragon (*Antirrhinum majus* genome ID Am04G23200.T01). The mixture was incubated overnight at 30 °C with shaking at 100 rpm. The reaction was stopped by adding 300 mL of a methanol:chloroform mixture (2:1, v/v). Subsequently, 100 mL of distilled water and 100 mL of chloroform were added, and the mixture was thoroughly mixed. The sample was then centrifuged at 10,000 ×*g* for 20 min at 4 °C, and the resulting supernatant was concentrated by freeze-drying. The *p*-coumaroyl-CoA produced in the reaction mixture was purified by preparative reversed-phase HPLC using a J'Sphere ODS M80 column (20 × 250 mm; YMC, Kyoto, Japan) at a flow rate of 5 mL/min. Solvent A was 0.1% (v/v) formic acid in H_2O, and solvent B was acetonitrile. Following a 5 mL injection onto the column, which was equilibrated with 10% (v/v) B, the column was initially developed isocratically with 10%B for 10 min, followed

by a linear gradient from 10% to 30%B over 60 min. The column was then washed isocratically with 90% B for 10 min and re-equilibrated with 10%B for 30 min before the next injection. Other chemicals used were of analytical grade.

Purification of PpCHS, PpCHIL, and PpCHS–PpCHIL and X-ray crystallography

N-terminally His_6-tagged PpCHS (Phytozome v12.1 locus name, Pp3c24_13120)[11] and PpCHIL (PpCHIL-B; Phytozome v12.1 locus name, Pp3c426_4040)[11] were independently overexpressed in *E. coli* BL21 (DE3) cells and purified as follows. The full-length PCR products containing the ORFs of PpCHS and PpCHIL were gel-purified and introduced into *Nde*I/*Bam*HI-digested pColdI, followed by verification of their nucleotide sequences. Resultant plasmids (termed PpCHS-pColdI and PpCHIL-pColdI) were introduced into *E. coli* BL21 (DE3) cells. The transformed cells were cultured in LB media supplemented with 100 μg/mL ampicillin (Nacalai Tesque, Kyoto, Japan) at 37 °C until their OD_{600} reached 0.5. Then the both cultures were cooled to 15 °C and kept for 30 min, followed by the additions of IPTG (final concentration, 0.2 mM). The cultivation were continued at 18 °C for 24 h, and the cultured cells were harvested by centrifugation. Harvested cells were disrupted and lysates were centrifuged (100,000 × *g* at 4 °C for 1 h). The supernatant was applied to a 10-mL column containing Ni-NTA agarose (FUJIFILM Wako Pure Chemical, Osaka, Japan) equilibrated with 50 mM Tris-HCl (pH 7.5) (Buffer A) containing 300 mM NaCl. The column was then washed with Buffer A containing 20 mM imidazole and proteins were eluted using Buffer A containing 200 mM imidazole. PpCHS was further purified using a HiTrap SP HP cation exchange column (5 mL; Cytiva, Marlborough, MA, USA), while PpCHIL was further purified using a HiTrap Q HP anion exchange column (5 mL; Cytiva). The HiTrap SP HP column was equilibrated with 20 mM MES-Na (pH 6.5), whereas the HiTrap Q HP column was equilibrated with 20 mM Tris-HCl (pH 7.5). Proteins from both columns were eluted using a linear gradient of NaCl from 0 to 1 M. Finally, proteins were purified using a size-exclusion chromatography column (HiLoad Superdex 200 16/60 pg; Cytiva) equilibrated with Buffer A containing 150 mM NaCl.

PpCHIL crystals were grown at 20 °C using the sitting-drop vapor diffusion method; 1 μL protein solution (15 mg/mL) was mixed with 1 μL well solution containing 100 mM Tris-HCl (pH 8.5), 100 mM $MgCl_2$, and 16%–20% PEG6000 or PEG8000. Typical crystals formed rhombus-shaped structures with an average length of 0.2 mm within 2 weeks. To determine the PpCHS-CoA structure, PpCHS crystals were grown at 20 °C using the sitting-drop vapor diffusion method; 1 μL protein solution (15 mg/mL) was mixed with 1 μL well solution containing 100 mM HEPES-Na (pH 7.5) and 16%–22% PEG3350. Typical crystals formed needle-like structures with an average length of 0.4 mm within 2 weeks. PpCHS crystals were then incubated with mother liquor containing 2.0 mM CoA-SH (Nacalai Tesque) and 37% PEG400 for 30 min at 20 °C before being flash-frozen in liquid nitrogen.

To isolate the PpCHS-PpCHIL complex, purified PpCHS and PpCHIL were mixed in equimolar amounts (120 μM each) and dialyzed overnight against Buffer A. The mixture was applied to a size-exclusion chromatography column (Superdex 200 Increase 15/300; Cytiva) equilibrated with Buffer A. Co-eluted fractions were pooled and concentrated using an Amicon Ultra (50 kDa MWCO; Merck KGaA, Darmstadt, Germany). PpCHS-PpCHIL crystals were grown at 20 °C using a sitting-drop vapor diffusion method; 1 μL protein solution (OD_{280} = 1.7) was mixed with 1 μL well solution containing 15.5% PEG3350 and 200 mM potassium citrate. Typical crystals formed needle-like structures with an average length of 0.5 mm within 1 week. X-ray diffraction data were collected at a wavelength of 1.00000 Å using an EIGER 9M detector (DECTRIS Ltd., Baden-Daettwil, Switzerland) on the BL32XU beamline equipped with the ZOO system at SPring-8, Harima, Japan[41]. Complete reflection data were obtained using a helical data collection scheme and then indexed and integrated with the KAMO pipeline using DIALS[42,43]. Integration intensities and data were merged using XSCALE, with outliers rejected using KAMO[44]. Structures were solved according to a molecular replacement method using Phaser[45], with an engineered chalcone isomerase (PDB: 5WKR) for PpCHIL and apo PpCHS (PDB: 6DX7) for PpCHS-CoA as search models. For the complex structure, we used a PpCHS-PpCHIL complex model determined by AlphaFold-Multimer v2.3.0[46,47]. Manual model building and

structure refinement were performed using COOT, REFMAC, and Phenix[48-50]. 3D molecular images were created using the PyMOL program (Schrödinger, L. & DeLano, W., 2020. PyMOL, Available at: http://www.pymol.org/pymol). Atomic coordinates and structural factors were deposited in the Protein Data Bank with PDB codes of 9KAH (PpCHS-PpCHIL), 9KAI (PpCHIL), and 9KAJ (PpCHS-CoA).

Computational docking studies

Docking simulations of CHS and CHIL from various plant species were performed using localcolabfold v1.5.5 from the AlphaFold2 program[51]. Essential flag options as well as three additional options were used: --amber, --use-gpu-relax, and --num-recycle 3.

Yeast two-hybrid assays

Yeast two-hybrid assays were completed using the Matchmaker Gold Yeast Two-Hybrid System (Clontech, Mountain View, CA, USA) as described previously[30-33]. Briefly, open reading frames encoding proteins to be tested were amplified by PCR to add SfiI restriction sites for the subsequent ligation to vectors pGBKT7 and pGADT7 (Clontech). Each amplified fragment was purified, digested with SfiI, and inserted into the SfiI site of pGBKT7 or pGADT7. *Saccharomyces cerevisiae* strain Y2H Gold (Clontech) cells were transformed with each plasmid pair according to the manufacturer's guidelines. For each 5-fold serially diluted cell suspension, 5 μL was placed on agar plates. Cells were grown at 30 °C for 2–4 days.

Site-directed mutagenesis

Mutated PpCHIL (T34A, E37Q, I38A, E39Q, F45A, K97A, and K100A), GmCHIL (T31A, E34Q, I35A, H36E, F42A, K93A, and K96A), and AtCHIL (E34Q, H36E, H36A, F37A, K94A, and K97A) were prepared using an overlapping extension PCR strategy as described previously[52] for yeast two-hybrid assays. The nucleotide sequences of the primers used for mutagenesis are presented in **Supplementary Table 4**.

MST analysis

The MST analysis conducted to examine the interaction between PpCHS and PpCHIL was performed using Monolith NT.115 (NanoTemper Technologies GmbH, Munich, Germany) and standard assay protocols[35,36]. PpCHS was labeled using Monolith His-Tag Labeling Kit RED-tris-NTA 2nd Generation (NanoTemper Technologies GmbH) according to the manufacturer's protocol. The labeled PpCHS and PpCHIL were dissolved in the MST analysis buffer containing 150 mM NaCl, 20 mM HEPES-NaOH (pH 7.0), and 0.1% Tween 20. PpCHS (70 nM) was used as a binding target for the MST analysis. As a ligand for the MST analysis, PpCHIL was titrated into the PpCHS solution in a 1:1 dilution series (0.53 mM to 0.016 μM). PpCHS and PpCHIL samples were mixed and loaded into a Monolith premium capillary (NanoTemper Technologies GmbH) and then MST fluorescence was measured at 25 °C using the MO.Control software bundled with Monolith NT.115. The excitation power was set at 78% and the MST power was set at medium. Data were analyzed using the MO.Affinity Analysis software (version 3.0.4; NanoTemper Technologies GmbH) under standard and default MST-on time conditions (4–5 s). F_{norm} (‰) represents the thousandth fraction of the normalized value of MST fluorescence before thermophoresis as 1. K_{d} was estimated by fitting the data using the following equation in the software:

$$f(c) = F_{\mathrm{unbound}} + (F_{\mathrm{bound}} - F_{\mathrm{unbound}}) \cdot \frac{c + c_{\mathrm{target}} + K_d - \sqrt{(c - c_{\mathrm{target}} + K_d)^2 - 4 \cdot c \cdot c_{\mathrm{target}}}}{2 \cdot c_{\mathrm{target}}}$$

where $f(c)$ is the fraction bound at a given ligand concentration c, F_{unbound} is the F_{norm} signal of the target alone, F_{bound} is the F_{norm} signal of the complex, and c_{target} is the final concentration of the target in the assay. K_{d} values were log-transformed and subjected to a one-way ANOVA with a Tukey–Kramer test, statistically analyzed using Excel (Microsoft), and expressed as the mean ± SD of three independent determinations.

Biolayer interferometry

Plasmids encoding the target proteins were constructed according to the manufacturer's instructions. The plasmid pColdI-Avi-PpCHS encodes a PpCHS fused at the *N*-terminus with a His_6-Avi tag (His_6-Avi-PpCHS), while pColdI-PpCHIL encodes a His_6-tagged PpCHIL protein (His_6-PpCHIL). The Avi tag is a 15-amino-acid peptide with the sequence GLNDIFEAQKIEWHE, which serves as a substrate for biotin ligase (BirA)-mediated biotinylation. For expression of His_6-Avi-PpCHS, *E. coli* strain AVB101 carrying pColdI-Avi-PpCHS was cultured in TYH medium supplemented with 100 μg/mL ampicillin and 0.5% glucose at 37 °C with shaking at 150 rpm. When the culture reached an OD_{600} of 0.3, biotin and IPTG were added to final concentrations of 50 μM and 1.5 mM, respectively, to induce biotinylation of His_6-Avi-PpCHS. The culture was further incubated at 37°C with shaking until the OD_{600} reached 0.6. Cells were then chilled on ice for 30 minutes and subsequently cultured overnight at 15 °C with shaking. For expression of His_6-PpCHIL, *E. coli* BL21 cells harboring pColdI-PpCHIL were grown in LB medium containing 100 μg/mL ampicillin at 37 °C with shaking until the OD_{600} reached 0.6. After chilling the culture on ice for 30 minutes, IPTG was added to a final concentration of 0.1 mM. The culture was then incubated overnight at 15 °C with shaking. Cells expressing either protein were harvested by centrifugation and stored at –30 °C until use. For cell lysis, the frozen pellets were resuspended in xTractor buffer (Takara Bio, Shiga, Japan) containing recommended concentrations of protease inhibitors, lysozyme, and DNase I. The lysate was clarified by centrifugation and the supernatant was filtered through a 0.45 μm membrane (Sartorius, Göttingen, Germany). Proteins were purified using immobilized metal affinity chromatography with a HisTrap HP column (Cytiva, Marlborough, MA, USA). Following purification, proteins were concentrated by ultrafiltration using Amicon Ultra-15 devices (Merck, Darmstadt, Germany), with a molecular mass cutoff of 30 kDa for biotinylated His_6-Avi-PpCHS and 10 kDa for His_6-PpCHIL. Buffer exchange was performed using ultrafiltration or gel filtration into 20 mM HEPES-KOH (pH 7.5) containing 50 mM NaCl. Glycerol was added to a final concentration of 20%, and the purified protein solutions were stored at –80 °C after flash-freezing in liquid nitrogen.

Protein–protein interaction measurements by biolayer interferometry[37] were performed using the Octet R2 System (Sartorius, Göttingen, Germany). Streptavidin biosensors were pre-equilibrated in assay buffer (100 mM HEPES-KOH, pH 7.5, containing 0.1% BSA) for at least 1 hour before use. Each biolayer interferometry assay was conducted in the assay buffer and consisted of the following steps: step 1, baseline 1 (0–60 s); step 2, loading of biotinylated His_6-Avi-PpCHS onto the streptavidin sensor (60–180 s); step 3, baseline 2 (180–240 s); step 4 (association phase), binding of His_6-PpCHIL to immobilized PpCHS (240–300 s); step 5 (dissociation phase), removal of His_6-PpCHIL from the biosensor (300–360 s). To assess non-specific binding, control BLI assays were performed in the absence of biotinylated PpCHS-Avi, following the same procedure. Control signals (from sensors loaded with PpCHS-Avi only) were subtracted from experimental values prior to data processing. To calculate the equilibrium dissociation constant (K_d) and the association (k_{on}) and dissociation (k_{off}) rate constants, sonsorgrams were fit to a 1:1 binding model using Octet Analysis Studio (version 13.0.1.35).

NMR spectroscopy

For resonance assignments of PpCHIL, NMR spectra were recorded using a Bruker AVANCE NEO 800 MHz NMR spectrometer equipped with a cryogenic probe [CPTCI(F)] (Bruker AVANCE III HD 500 MHz equipped with BBO) (Bruker, Billerica, MA, USA). All NMR spectra were processed using the NMRPipe program[53] and TopSpin, after which data were analyzed using SPARKY or POKY[54]. Standard spectral sets for ^{13}C- and ^{15}N-labeled PpCHIL (0.3 mM) dissolved in a solution containing 25 mM potassium phosphate pH 7.0, 150 mM NaCl, 0.5 mM EDTA, 1 mM PMSF, and 10% ^2H_2O were used for backbone resonance assignment. The following spectral sets were used: [^1H-^{15}N] HSQC, HNCO, HN(CO)CA, HNCA, CBCA(CO)NH, HNCACB, HBHA(CO)NH, C(CO)NH, and N-NOESY (mixed for 150 ms).

For titration experiments, ^{15}N-labeled CHIL (0.2 mM) was dissolved in a solution containing 25 mM potassium phosphate pH 7.0, 0 or 50 mM NaCl, and 10% ^2H_2O. NMR spectra were obtained using a Bruker AVANCE 500 MHz equipped with a BBFO probe.

The sample temperature was set at 25 °C. The ^{15}N-TROSY HSQC pulse sequence was used to obtain the backbone ^{1}H-^{15}N correlation spectrum. Non-labeled PpCHS (1 mM) was titrated into the ^{15}N-labeled PpCHIL solution at molar ratios of 0.2, 0.5, and 1. Data were processed using NMRPipe[53], whereas spectra were analyzed using POKY[54]. The chemical shift perturbation (CSP) of the backbone amide group was averaged using the following equation:

$$\mathrm{CSP} = \sqrt{\Delta\delta_{\mathrm{H}}^2 + (\frac{\Delta\delta_{\mathrm{N}}}{5})^2}$$

where $\Delta\delta_{\mathrm{H}}$ and $\Delta\delta_{\mathrm{N}}$ represent the chemical shift changes of the proton and nitrogen, respectively.

Simulation protocols

Covalent docking simulation were performed for modeling of T-i covalently bound to Cys170$^{\mathrm{PpCHS}}$. The initial protein models were generated from crystal structures. The T-i ligand was drawn and structurally optimized using Chem3D with the MM2 force field. One hundred trial simulations were performed independently, and the structure with the lowest binding energy was used for the following MD simulations. Covalent docking of T-i to CHS was performed using AutoDock-GPU and MGLTools, treating T-i as the only flexible molecule.

Quantum chemical calculations were performed to determine the force field parameters of T-i used in the following MD simulations. After geometry optimization of T-i, ESP charges were calculated using the Hartree-Fock method with 6-31G(d) basis set by Gaussian 16. Antechamber package was used to prepare the parameters of T-i for the MD simulations.

MD simulations were carried out to investigate the structure and dynamics of protein complexes. We prepared three simulation systems, that is, PpCHS, PpCHS-PpCHIL, and PpCHS-CoA in aqueous solution. All systems include the T-i covalently bound to

Cys170^{PpCHS} obtained from the docking simulation as described above. The initial configurations of each crystal structure were prepared by solvating with water molecules. To neutralize the total charge of the system, Na^+ and Cl^- ions were added to a concentration of 150 mM. The total number of atoms in the PpCHS, PpCHS-PpCHIL, and PpCHS-CoA systems were 111482, 135286, and 115941 atoms, respectively. Then, a two-step energy minimization was performed with and without harmonic constraints on the position of heavy atoms using a force constant of 1000 kJ/mol·nm^2. In the subsequent equilibration MD simulation, the harmonic constraints were gradually weakened and finally removed within 1.8 ns. Then production run was carried out at 300 K and 0.1 MPa using velocity rescaling[55] and isotropic Parrinello-Rahman[56,57], respectively. The cut-off distance for the calculation of long-range interactions was set to 1.0 nm. Electrostatic interactions were calculated using the Particle Mesh Ewald method[58,59]. AMBER ff14SB[60] and TIP3P[61] force fields were applied to describe amino acid residues and water molecules, respectively. All simulations were performed using GROMACS version 2025.1[39].

Enzyme assays

The standard enzyme assay mixture (final volume, 50 μL) consisted of 100 mM HEPES-NaOH buffer (pH 7.5), 50 μM *p*-coumaroyl-CoA, 100 μM malonyl-CoA, PpCHS (typically 0.1 μM), and PpCHIL (typically 1.0 μM). The mixture, excluding PpCHS, was pre-incubated at 30 °C for 5 min, and the reaction was initiated by adding PpCHS. After a 60-min incubation at 30 °C, the reaction was terminated by adding 50 μL of a mixture containing acetonitrile and water (2:3, v/v) and 4% (v/v) formic acid. Flavonoids and related products formed in the reaction mixture were analyzed by reversed-phase HPLC using an L-column3 C18 column (2 μm, 2.1 × 50 mm; Chemicals Evaluation and Research Institute, Tokyo, Japan) on a Thermo Scientific Vanquish Core HPLC system. Solvent A was 0.1% (v/v) formic acid in water, and solvent B was acetonitrile. A 10 μL aliquot of the reaction mixture was injected onto the column, which had been equilibrated with 10% B. The column was then developed isocratically for 0.5 min, followed by a linear gradient from 10% to 50% B over 6 min. Subsequently, the column was washed isocratically with

90% B for 0.5 min and re-equilibrated with 10% B for 3 min before the next injection. Chromatograms were recorded with a diode array detector, and quantification was performed at 290 nm for naringenin, 330 nm for CTAL, and 370 nm for THC.

Enzyme kinetics

Initial velocity assays of the CHS-catalyzed reactions were performed using the standard assay system (described above) under steady-state conditions with varying substrate concentrations. The apparent Michaelis constant (K_m) and maximum velocity (V_{max}) values, along with their standard errors, for either *p*-coumaroyl-CoA or malonyl-CoA (in the presence of a fixed concentration of the other substrate) were determined by fitting the initial velocity data to the Michaelis–Menten equation using a nonlinear regression method in SigmaPlot 12 (Hulinks, Tokyo, Japan).

Reporting summary

Further information on research design is available in the Nature Portfolio Reporting Summary linked to this rticle.

Data availability

Crystal structures are available in PDB under the following ID numbers: PpCHS–CoA complex, 9KAJ; PpCHIL, 9KAI; PpCHS–PpCHIL complex, 9KAH. All other data are available in the main text or the supplementary materials.

References

1. Srere, P. A. The Metabolon. *Trends Biochem. Sci.* **10**, 109–110 (1985).
2. Bassard, J. E. & Halkier B. A. How to prove the existence of metabolons? *Phytochem. Rev.* **17**, 211–227 (2018).
3. Srere, P. A. Macromolecular interactions: tracing the roots. *Trends Biochem. Sci.* **25**, 150–153 (2000).

4. Chehade, M. H. et al. A soluble metabolon synthesizes the isoprenoid lipid ubiquinone. *Cell Chem. Biol.* **26**, 482–492 (2019).
5. Pedley, A. M., Pareek, V. & Benkovic, S. J. The purinosome: a case study for a mammalian metabolon. *Annual Rev. Biochem.* **91**, 89–106 (2022).
6. Obata, T. Metabolons in plant primary and secondary metabolism. *Phytochem. Rev.* **18**, 1483–1507 (2019).
7. Dahmani, I., Qin, K. Z., Zhang, Y. J. & Fernie, A. R. The formation and function of plant metabolons. *Plant J.* **114**, 1080–1092 (2023).
8. Saks, V., Beraud, N. & Wallimann, T. Metabolic compartmentation - a system level property of muscle cells: real problems of diffusion in living cells. *Int. J. Mol. Sci.* **9**, 751–767 (2008).
9. Ovadi, J. Physiological significance of metabolic channelling. *J. Theor. Biol.* **152**, 1–22 (1991).
10. Zhang, Y. & Fernie, A. R. Metabolons, enzyme-enzyme assemblies that mediate substrate channeling, and their roles in plant metabolism. *Plant Commun.* **2**, 100081 (2020).
11. Waki, T. *et al.*, A conserved strategy of chalcone isomerase-like protein to rectify promiscuous chalcone synthase specificity. *Nat. Commun.* **11**, 870 (2020).
12. Waki, T., Takahashi, S. & Nakayama, T. Managing enzyme promiscuity in plant specialized metabolism: A lesson from flavonoid biosynthesis: Mission of a "body double" protein clarified. *BioEssays*, e2000164 (2020).
13. Bassard, J. E., Moller, B. L. & Laursen, T. Assembly of dynamic P450-mediated metabolons-order versus chaos. *Curr. Mol. Biol. Rep.* **3**, 37–51 (2017).
14. Winkel-Shirley, B. Flavonoid biosynthesis. A colorful model for genetics, biochemistry, cell biology, and biotechnology. *Plant Physiol.* **126**, 485–493 (2001).
15. Yonekura-Sakakibara, K., Higashi, Y. & Nakabayashi, R. The origin and evolution of plant flavonoid metabolism. *Front. Plant Sci.* **10**, 943 (2019).

16. Wiseman, H. "Isoflavonoids and human health" in *Flavonoids: Chemistry, Biochemistry and Applications,* Ø. Andersen, K. Markham, Eds. (CRC Press, Taylor & Francis, Boca Raton, FL, 2006), pp. 371–396.
17. Austin, M. B. & Noel, J. P. The chalcone synthase superfamily of type III polyketide synthases. *Nat. Prod. Rep.* **20**, 79–110 (2003).
18. Imaizumi, R. et al. Crystal structure of chalcone synthase, a key enzyme for isoflavonoid biosynthesis in soybean. *Proteins Struct. Funct. Bioinfo.* **89**, 126–131 (2021).
19. Burbulis, I. E. & Winkel-Shirley, B. Interactions among enzymes of the *Arabidopsis* flavonoid biosynthetic pathway. *Proc. Natl. Acad. Sci. USA*, **96**, 12929–12934 (1999).
20. Winkel-Shirley, B. Evidence for enzyme complexes in the phenylpropanoid and flavonoid pathways. *Physiol. Plant.* **107**, 142–149 (1999).
21. Nakayama, T., Takahashi, S. & Waki, T. Formation of flavonoid metabolons: functional significance of protein-protein interactions and impact on flavonoid chemodiversity. *Front. Plant Sci.* **10**, 821 (2019).
22. Weng, J. K. & Noel, J. P. The remarkable pliability and promiscuity of specialized metabolism. *Cold Spring Harb. Symp. Quant. Biol.* **77**, 309–320 (2012).
23. Moghe, G. D. & Last, R. L. Something old, Something new: conserved enzymes and the evolution of novelty in plant specialized metabolism. *Plant. Physiol.* **169**, 1512–1523 (2015).
24. Waki, T. et al. Structural insights into catalytic promiscuity of chalcone synthase from *Glycine max* (L.) Merr.: Coenzyme A-induced alteration of product specificity. *Biochem. Biophys. Res. Commun.* **718**, 150080 (2024).
25. Morita, Y. et al. A chalcone isomerase-like protein enhances flavonoid production and flower pigmentation. *Plant J.* **78**, 294–304 (2014).
26. Jiang, C., Schommer, C. K., Kim, S. Y. & Suh, D. Y. Cloning and characterization of chalcone synthase from the moss, *Physcomitrella patens*. *Phytochemistry* **67**, 2531–2540 (2006).

27. Wolf-Saxon, E. R. et al. Regulatory ligand binding in plant chalcone isomerase-like (CHIL) proteins. *J. Biol. Chem.* **299**, 104804 (2023).
28. Liou, G. et al. Mechanistic basis for the evolution of chalcone synthase catalytic cysteine reactivity in land plants. *J. Biol. Chem*. **293**, 18601-18612 (2018).
29. Barthels, F., Schirmeister, T. & Kersten, C. BANΔIT: B'-factor analysis for drug design and structural biology. *Mol. Inform.* **40**, e20001442021 (2021).
30. Chien, C. T. et al. The two-hybrid system: a method to identify and clone genes for proteins that interact with a protein of interest. *Proc. Natl. Acad. Sci. USA* **88**, 9578–9582 (1991).
31. Fujino, N. et al. Physical interactions among flavonoid enzymes in snapdragon and torenia reveal the diversity in the flavonoid metabolon organization of different plant species. *Plant J*. **94**, 372–392 (2018).
32. Waki, T. et al. Identification of protein-protein interactions of isoflavonoid biosynthetic enzymes with 2-hydroxyisoflavanone synthase in soybean (*Glycine max* (L.) Merr.). *Biochem. Biophys. Res. Commun*. **469**, 546–551 (2016).
33. Mameda, R. et al. Involvement of chalcone reductase in the soybean isoflavone metabolon: identification of GmCHR5, which interacts with 2-hydroxyisoflavanone synthase. *Plant J.* **96**, 56–74 (2018).
34. Blumwald, E., Aharon, G. S. & Apse, M. P. Sodium transport in plant cells. *Biochim. Biophys. Acta-Biomembranes* **1465**, 140–151 (2000).
35. Hill, C. H. et al. Structural and molecular basis for cardiovirus 2A protein as a viral gene expression switch. *Nat. Commun.* **12**, 7166 (2021).
36. Jerabek-Willemsen, M. et al. MicroScale thermophoresis: interaction analysis and beyond. *J. Mol. Struct.* **1077**, 101–113 (2014).
37. Abdiche, Y. et al. Determining kinetics and affinities of protein interactions using a parallel real-time label-free biosensor, the Octet. *Anal. Biochem.* **377**, 209–217 (2008).
38. Santos-Martins, D. et al. Accelerating AutoDock4 with GPUs and gradient-based local search. *J. Chem. Theor. Comput.* **17**, 1060–1073 (2021).

716 39. Abraham, M. J. et al. GROMACS: High performance molecular simulations through
717 multi-level parallelism from laptops to supercomputers. *SoftwareX*, **1–2** 19–25 (2015).
718 40. Wu, F. & Minteer, S. Krebs cycle metabolon: structural evidence of substrate
719 channeling revealed by cross-linking and mass spectrometry. *Angew. Chem. Int. Ed.*
720 **54,**1851–1854 (2015).
721 41. Hirata, K. et al. ZOO: an automatic data-collection system for high-throughput
722 structure analysis in protein microcrystallography. *Acta Crystallogr. D* **75**, 138–150
723 (2019).
724 42. Yamashita, K., Hirata, K. & Yamamoto, M. KAMO: towards automated data
725 processing for microcrystals. *Acta Crystallogr. D* **74**, 441–449 (2018).
726 43. Kabsch, W. Integration, scaling, space-group assignment and post-refinement. *Acta*
727 *Crystallogr. D-Biol. Crystallogr.* **66**, 133–144 (2010).
728 44. Matsuura, H. et al. Elucidating polymorphs of crystal structures by intensity-based
729 hierarchical clustering analysis of multiple diffraction data sets. *Acta Crystallogr. D*
730 **79**, 909–924 (2023).
731 45. McCoy, A. J. Solving structures of protein complexes by molecular replacement with
732 Phaser. *Acta Crystallogr. D* **63**, 32–41 (2007).
733 46. Jumper, J. et al., Highly accurate protein structure prediction with AlphaFold. *Nature*
734 **596**, 583–589 (2021).
735 47. Evans, R. et al. Protein complex prediction with AlphaFold-Multimer. *BioRxiv* (2021)
736 doi: 10.1101/2021.10.04.463034v12 .
737 48. Emsley, P., Lohkamp, B., Scott, W. G. & Cowtan, K. Features and development of
738 Coot. *Acta Crystallogr. D-Biol. Crystallogr.* **66**, 486–501 (2010).
739 49. Murshudov, G. N. et al. REFMAC5 for the refinement of macromolecular crystal
740 structures. *Acta Crystallogr. D* **67**, 355–367 (2011).
741 50. Afonine, P. V. et al. Real-space refinement in PHENIX for cryo-EM and
742 crystallography. *Acta Crystallogr. D* **74**, 531–544 (2018).
743 51. Mirdita, M. et al. ColabFold: making protein folding accessible to all. *Nat. Methods* **19**,
744 679–682 (2022).

52. Okegawa, Y. & Motohashi, K. A simple and ultra-low cost homemade seamless ligation cloning extract (SLiCE) as an alternative to a commercially available seamless DNA cloning kit. *Biochem. Biophys. Rep.* **4**, 148–151 (2015).
53. Delaglio, F. et al. NMRPipe: A multidimensional spectral processing system based on UNIX pipes. *J. Biomol. NMR* **6**, 277–293 (1995).
54. Lee W. et al. POKY: a software suite for multidimensional NMR and 3D structure calculation of biomolecules. *Bioinformatics* **37**, 3041–3042 (2021).
55. Bussi, G., Donadio, D. & Parrinello, M. Canonical sampling through velocity rescaling. *J. Chem. Phys.* **126,** 014101 (2007).
56. Parrinello, M. & Rahman, A. Polymorphic transitions in single crystals: A new molecular dynamics method. *J. Appl. Phys*. **52,** 7182–7190 (1981).
57. Nosé, S. & Klein, M. L. Constant pressure molecular dynamics for molecular systems. *Mol. Phys*. **50,** 1055–1076 (1983).
58. Darden, T., York, D. & Pedersen, L. Particle mesh Ewald: An N-log(N) method for Ewald sums in large systems. *J. Chem. Phys*. **98,** 10089–10092 (1993).
59. Essmann U. et al. A smooth particle mesh Ewald method. *J. Chem. Phys*. **103,** 8577–8593 (1995).
60. Maier J. A. et al. ff14SB: Improving the accuracy of protein side chain and backbone parameters from ff99SB. *J. Chem. Theor. Comput.* **11,** 3696–3713 (2015).
61. Jorgensen, W. L. et al. Comparison of simple potential functions for simulating liquid water. *J. Chem. Phys.* **79**, 926–935 (1985).
62. Watkinson, J. I. et al. Identification of MOS9 as an interaction partner for chalcone synthase in the nucleus. *Peer J*. **6,** e5598 (2018).

Acknowledgements

We thank the SPring-8 staff members for their help with the BL32XU beamline and X-ray diffraction experiments. This work is supported by JSPS KAKENHI grant numbers 18H03938, 20K15448, 21H02115, 21J22186, 22KJ1466, 23H05470, and 24K23286. This work is also supported by Platform Project for Supporting Drug Discovery and Life

Science Research [Basis for Supporting Innovative Drug Discovery and Life Science Research (BINDS)] from AMED under grant number JP20am0101070 (support number 1841) and Bio-SPMs Collaborative Research of the WPI Nano Life Science Institute (WPI-NanoLSI, Kanazawa University). We also thank Mark Cleasby, PhD from Edanz (https://jp.edanz.com/ac) for editing a draft of this manuscript.

Author contributions

Conceptualization: SY, TW, TNakayama; Methodology: RI, TW, YH, KT, KKawaguchi, HM, TYokoyama, RO, KN, NS, TS, YT, NK, MY; Investigation: RI, TW, YH, MS, KT, KKawaguchi, HK, KS, YK, YD, AY, TNakano, KUno, KY, MT, ST, KKataoka; Visualization: YH, TYanai, KKawaguchi, KUmeda, RO, KN, TS, YT, NK, SY; Funding acquisition: NK, SY, MY, TNakayama,; Project administration: SY, TW; Supervision: TNakayama, MY, KKataoka; Writing – original draft: SY, TNakayama; Writing – review & editing: ST, KKataoka, NK, TS, YT.

Competing interests

Authors declare that they have no competing interests.

Additional information

Supplementary information The online version contains supplementary materials (Supplementary Figs. 1 to 16, Supplementary Tables 1 to 4, Supplementary Notes 1 and 2) available at:

Fig. 1:

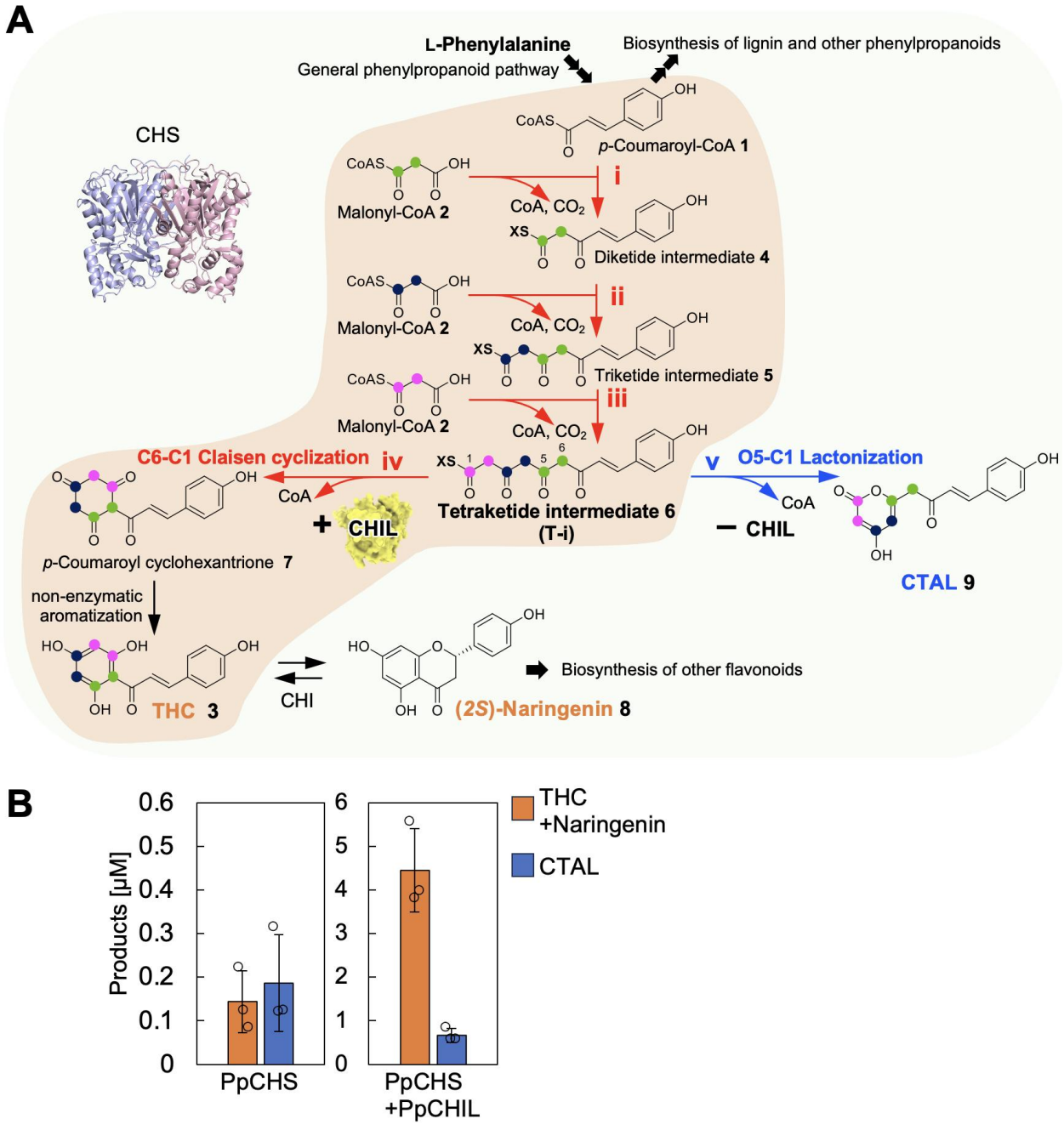


Fig. 1. Chalcone synthase (CHS)-catalyzed reactions, and the effect of chalcone isomerase-like protein (CHIL) on the product specificity of CHS. (A) Pathways

803 involving CHS-catalyzed reactions and the related processes. The CHS-catalyzed
804 production of 2′,4,4′,6′-tetrahydroxychalcone (THC) is presented on an orange
805 background. The THC-generating pathway is indicated by red arrows (i–iv) and the
806 derailment pathway producing *p*-coumaroyl-triacetic acid lactone (CTAL) is indicated by a
807 blue arrow (v). CHIL (yellow) binds to CHS (upper left) to increase THC production and
808 reduce CTAL formation. *p*-Coumaroyl-CoA is delivered *via* the general phenylpropanoid
809 pathway and also serves as a precursor for the biosynthesis of lignin and other
810 phenylpropanoids (thick downward and upward arrows). THC is converted to (2*S*)-
811 naringenin by chalcone isomerase, leading to the production of various flavonoid classes, as
812 indicated by a rightward thick arrow. **T-i**, tetraketide intermediate; **X,** CoA- or enzyme
813 Cys-. **(B**) Effect of PpCHIL on the product specificity of PpCHS. PpCHS (0.1 μM) was
814 analyzed as described previously[11,24] in the absence (left panel) and presence (right panel)
815 of PpCHIL (1.0 μM). Because THC is nonenzymatically isomerized to produce naringenin,
816 the THC-producing activity of PpCHS was quantified using the total amounts of THC and
817 naringenin (collectively termed chalconoids (CLC)).
818

Fig. 2:

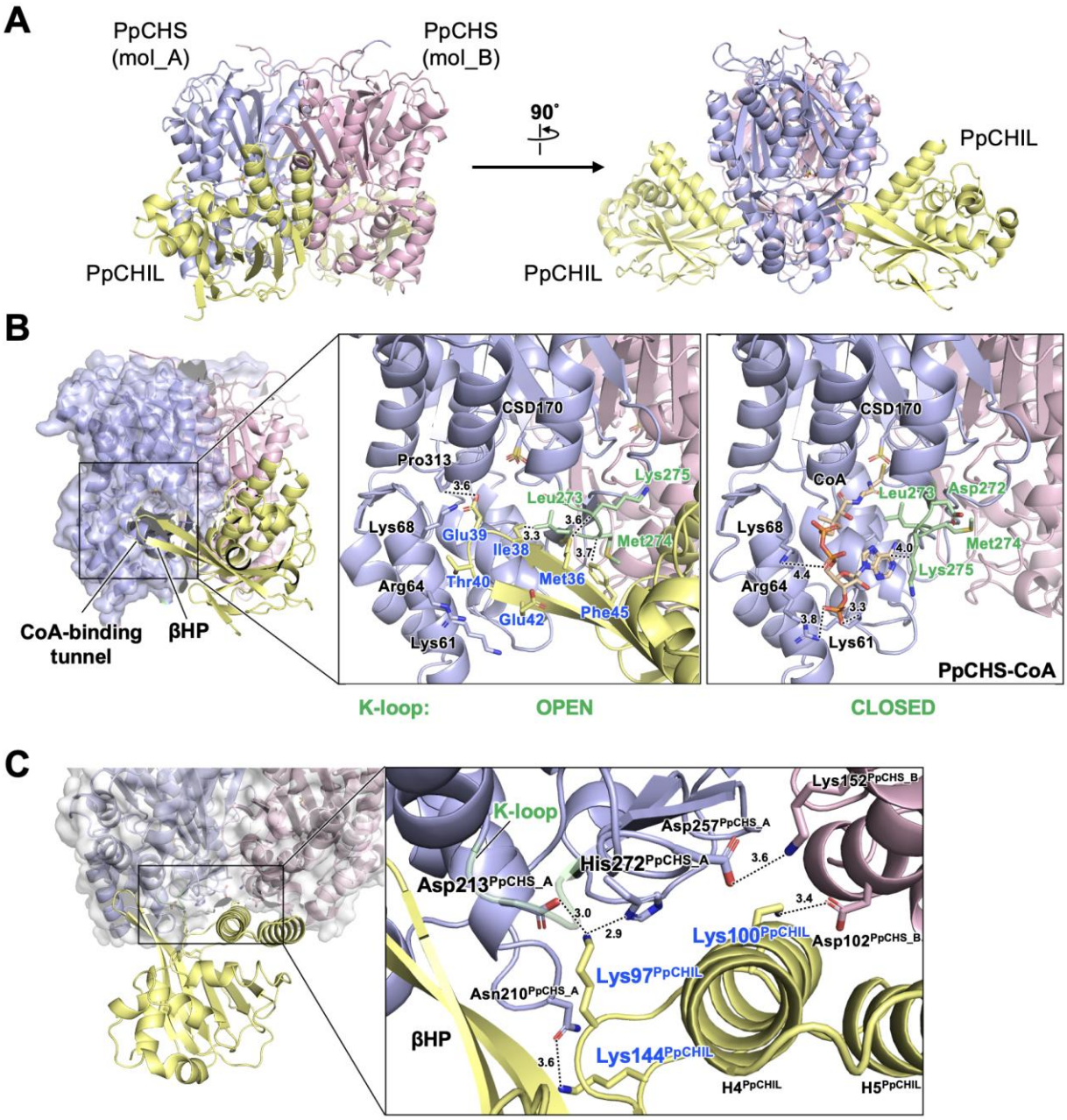


Fig. 2. Structure of the PpCHS–PpCHIL complex. (**A**) Crystal structure of the PpCHS–PpCHIL complex, showing that in the 2:2 assembly, each PpCHIL monomer simultaneously binds to both subunits of the PpCHS dimer. (**B**) Left panel: binding of PpCHIL (yellow) to the CoA-binding tunnel of PpCHS [overlapping ribbon (purple) and

surface (purple) models]. The center panel presents a close-up view of the contact interface. Residues of the K-loop are labeled with green text. Amino acid residues in the βHP of PpCHIL are labeled with blue text. Right: close-up view of the portion corresponding to that shown in the center panel in the binary PpCHS–CoA complex (PDB:9KAJ). CSD170, catalytic cysteine sulfinic acid 170[18]. Possible ionic interactions or other interactions are indicated by dotted lines; distances are given in Å. (**C**) Left panel: contact interface area between PpCHIL (yellow) and PpCHS (mol_A in purple and mol_B in pink). Right panel: ionic interactions of $Lys97^{PpCHIL}$ with $Asp213^{PpCHS_A}$ and $His272^{PpCHS_A}$ near the K-loop (green) of PpCHS are indicated by dotted lines. The salt bridges formed between $Lys100^{PpCHIL}$ on helix $H4^{PpCHIL}$ and $Asp102^{PpCHS_B}$ and between $Asp257^{PpCHS_A}$ and $Lys152^{PpCHS_B}$ are also indicated by dotted lines. The numbers beside the dotted lines are distances in Å.

Fig. 3:

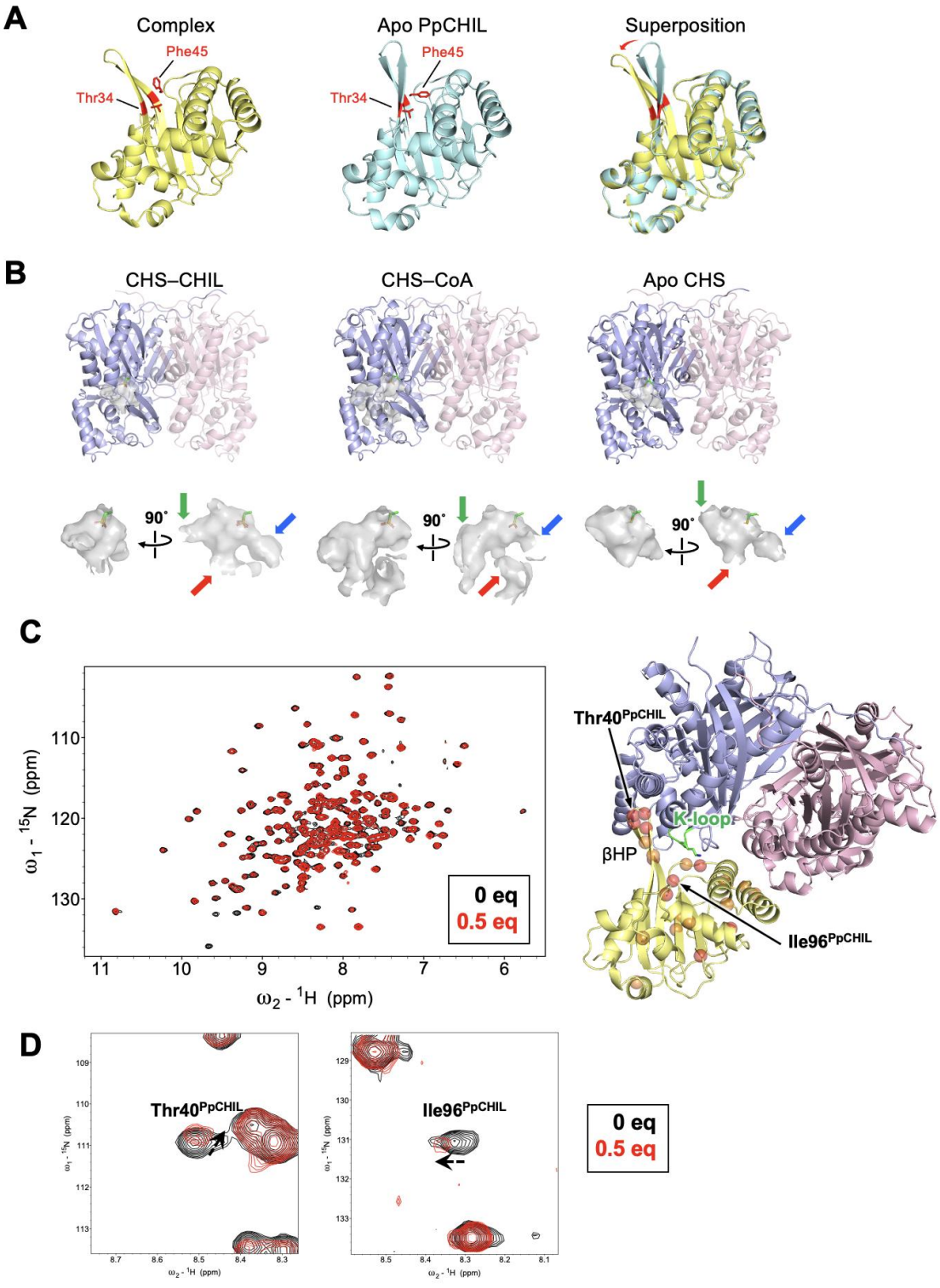

A
Complex
Phe45
Thr34
Apo PpCHIL
Phe45
Thr34
Superposition
B
CHS–CHIL
CHS–CoA
Apo CHS
90˚
90˚
90˚
C
ω1 - 15N (ppm)
110
120
130
ω2 - 1H (ppm)
11
10
9
8
7
6
0 eq
0.5 eq
Thr40PpCHIL
K-loop
βHP
Ile96PpCHIL
D
Thr40PpCHIL
Ile96PpCHIL
0 eq
0.5 eq

Fig. 3. Structural alterations of PpCHS–PpCHIL complex components (X-ray crystallography) and complex dynamics (NMR analysis). (**A**) PpCHIL structures: PpCHIL from the PpCHS–PpCHIL complex, alone, and a superposition, emphasizing the movement of the βHP region (red arrow; $Thr34^{PpCHIL}$, $Phe45^{PpCHIL}$ highlighted in red). (B) PpCHS structures: comparison of PpCHS from the PpCHS–PpCHIL complex and the PpCHS–CoA complex and apo PpCHS. The active-site cavity (transparent gray surface) is enlarged below, with arrows pointing to the CoA-binding tunnel (green), chalconoid (CLC)-binding pocket (blue), and tunnel-like space (red). The catalytic Cys170 stick structure is shown. (**C**) NMR titration analysis. Left: superposition of ^{1}H-^{15}N HSQC spectra of ^{15}N-labeled PpCHIL with (red) and without (black) 0.5 equivalents (eq) PpCHS in the presence of 50 mM NaCl. Right: chemical shift perturbation (CSP) mapping of the structure of the PpCHS–PpCHIL complex. Cutoffs for the chemical shift perturbation mapping were determined using $\Delta\delta_{ave} + \Delta\delta_{SD}$ (orange spheres) and $\Delta\delta_{ave} + 2\Delta\delta_{SD}$ (red spheres), where $\Delta\delta_{ave}$ and $\Delta\delta_{SD}$ are the mean and standard deviation, respectively, of the chemical shift change after the ligand was added. (**D**) Close-up views of CSP for the residues $Thr40^{PpCHIL}$ (left) and $Ile96^{PpCHIL}$ (right).

Fig. 4:

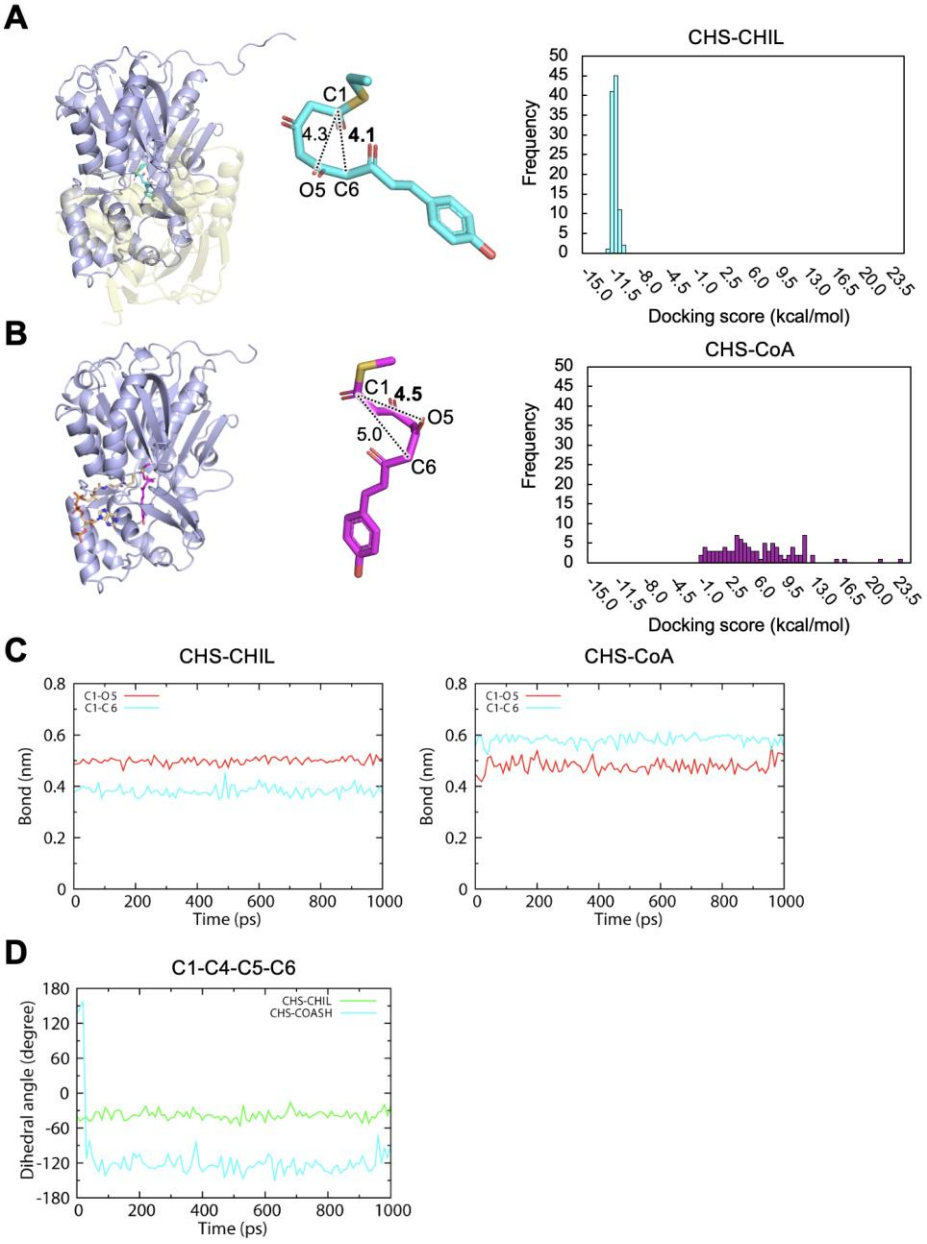


Fig. 4. Computational simulations of T-i conformation dynamics within protein complexes. Covalent docking results (left), the conformations of covalently bound T-i (center), and the docking scores (right) for the PpCHS–PpCHIL complex (**A**) and PpCHS–

CoA (**B**). (**C**) Time-dependent changes in distances between C6–C1 (blue) and O5–C1 (red) during 1,000-ps MD simulations (left: PpCHS–PpCHIL; right: PpCHS–CoA). (**D**) Dihedral angle analysis of carbon atoms (C1–C4–C5–C6) in T-i across two PpCHS states (green: PpCHS–PpCHIL; blue: PpCHS–CoA). When the dihedral angle is 0°, C6–C1 Claisen cyclization is particularly favored.

Fig. 5:

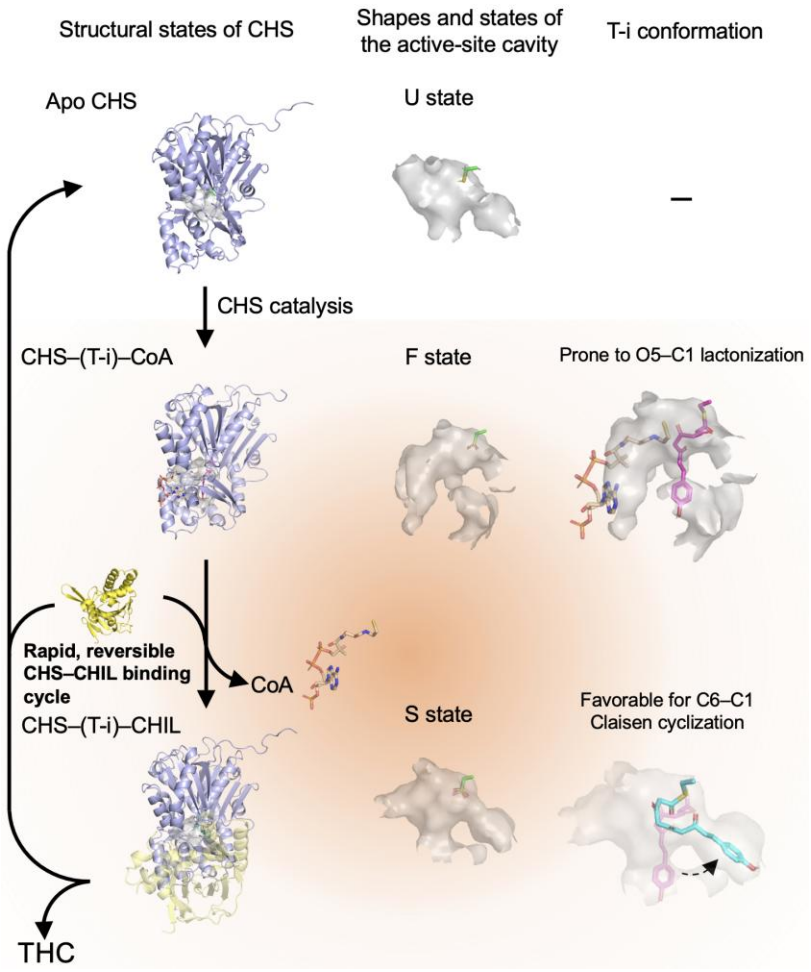


Fig. 5. Guided Active-site Tuning via Transient Enzyme Association (GATE): an illustration using the CHIL-CHS system. This figure illustrates the GATE effect using the CHIL-CHS system. Protein structures (CHS: purple; CHIL: yellow) are shown as ribbons, with the active-site cavity as a gray surface. T-i and CoA are shown as stick structures. The process begins with the formation of the CHS–(T-i)–CoA state (orange background). Here, T-i (magenta) is linked to the catalytic cysteine, and CoA occupies its binding tunnel. The active site is structurally flexible (F state), causing T-i to adopt an unstable conformation that favors O5–C1 lactonization. CHS then transiently and

884 reversibly associates with CHIL, a process that is 100-1000 times faster than catalysis. This
885 association displaces CoA, forming the novel CHS–(T-i)–CHIL state. In this new state, the
886 active-site cavity becomes structurally stable (S state). This stability precisely repositions
887 T-i (light blue) into the CLC-binding pocket, forcing it into a stable conformation that is
888 optimally suited for productive C6–C1 Claisen cyclization.
889

Supplementary Files

This is a list of supplementary files associated with this preprint. Click to download.

- 03supplementaryinformation.pdf